

5. Union Carbide Corporation, Carbon Products Division (now AMOCO Performance Products), Technical Information Bulletins 465-223, 465-225, 465-246.
6. P. Wagner, *J. Am. Ceramic Soc.*, **55**, 214 (1971).
7. O. M. Baycure, *IEEE Trans. Indust.*, **5**, 208 (1968).
8. K. Kinoshita and S. C. Leach, *This Journal*, **129**, 1993 (1982).
9. "Chemical Engineers Handbook," 5th ed., R. H. Perry and C. H. Chilton, McGraw-Hill, New York (1973).
10. W. L. Ingmanson *et al.*, *TAPPI*, **42**, 840 (1959).

## Polymer Electrolyte Fuel Cell Model

T. E. Springer,\* T. A. Zawodzinski,\* and S. Gottesfeld\*

Los Alamos National Laboratory, Los Alamos, New Mexico 87545

### ABSTRACT

We present here an isothermal, one-dimensional, steady-state model for a complete polymer electrolyte fuel cell (PEFC) with a 117 Nafion® membrane. In this model we employ water diffusion coefficients, electro-osmotic drag coefficients, water sorption isotherms, and membrane conductivities, all measured in our laboratory as functions of membrane water content. The model predicts a net-water-per-proton flux ratio of  $0.2 \text{ H}_2\text{O}/\text{H}^+$  under typical operating conditions, which is much less than the measured electro-osmotic drag coefficient for a fully hydrated membrane. It also predicts an increase in membrane resistance with increased current density and demonstrates the great advantage of a thinner membrane in alleviating this resistance problem. Both of these predictions were verified experimentally under certain conditions.

Fuel cells employing hydrated Nafion or other hydrated perfluorinated ionomeric materials as the electrolyte are promising candidates for electric vehicle applications (1). The polymer electrolyte provides room temperature start-up, elimination of many corrosion problems, and the potential for low resistance losses. Resistive losses within the fuel cell result, in part, from the decrease of membrane protonic conductivity following partial dehydration of the membrane. On the other hand, cathode flooding problems are caused when too much water is in the system. Clearly, water management within the fuel cell involves walking a tightrope between the two extremes.

Spatial variations of water content within the polymeric electrolyte of a current-carrying fuel cell result from the electro-osmotic dragging of water with proton transport from anode to cathode, the production of water by the oxygen reduction reaction at the cathode, humidification conditions of the inlet gas streams, and "back-diffusion" of water from cathode to anode, which lessens the concentration gradient.

The water distribution within a polymer electrolyte fuel cell (PEFC) has been modeled at various levels of sophistication by several groups. Verbrugge and Hill (2-4) have carried out extensive modeling of transport properties in perfluorosulfonate ionomers based on dilute solution theory. Fales *et al.* (5) reported an isothermal water map based on hydraulic permeability and electro-osmotic drag data. Though the model was relatively simple, some broad conclusions concerning membrane humidification conditions were reached. Fuller and Newman (6) applied concentrated solution theory and employed literature data on transport properties to produce a general description of water transport in fuel cell membranes. The last contribution emphasizes water distribution within the membrane. Boundary values were set in these cases rather arbitrarily. A different approach was taken by Bernardi (7). She considered transport through the gas diffusion electrodes, assuming the membrane to be uniformly hydrated, corresponding to an "ultrathin membrane" case.

We present an isothermal, one-dimensional, steady-state model for water transport through a complete PEFC. The model includes transport through the porous electrodes, based on calculated diffusivities corrected for porosity, and transport through the membrane electrolyte, based on experimentally determined transport parameters. In this model, we employ water-diffusion coefficients, electro-osmotic drag coefficients, water sorption isotherms, and membrane conductivities, all of which are measured in our laboratory as functions of membrane water content. We deemed it highly desirable to use in our model a complete

set of experimental data generated under conditions in which the membrane is routinely handled (for example, pretreated) and tested for PEFC work as consistently as possible. Furthermore, we explicitly measured parameters over the fullest possible range of water contents to enable us to include the effects of the variation of water content as a function of position within the membrane during any current flow.

### General Aspects of the Model

The distribution of water in a PEFC at steady state (constant current and fluxes) is calculated in this model by considering water flow through the following five regions of unit cross-sectional area within the fuel cell, as schematically illustrated in Fig. 1: the two inlet channels, the two gas diffusion electrodes, and the Nafion membrane. Not only does water enter the fuel cell assembly as a component of the humidified fuel and oxidant streams, but water is also generated at the cathode by the oxygen reduction reaction. We entered into the model the cell current, cell and humidifier temperatures, anode and cathode pressures, inlet gas flow rates, and oxygen/nitrogen ratio in the cathode gas feed. The cell is considered isothermal between the inlet channels.

The water flow into the inlet channels is set by the temperatures of the external gas humidifiers and the cell. Water vapor is equilibrated at the saturation pressures set by the humidifier temperatures in the inlet flow streams. Entrained droplets may be considered to form and be transported with the flow stream if the cell temperature is less than the humidifier temperature. These droplets will re-evaporate in the inlet flow channels if the condition of the assumed thoroughly mixed fluid there become less than saturation. Under these isothermal, thoroughly mixed or mean conditions, the model can use entrained droplets as a transport mechanism for water without having to specify the details. We will discuss elsewhere a qualitative treatment of electrode "flooding" (large excess of liquid water) when it occurs. Water vapor leaves the two inlet flow channels at the mean mole fraction of the respective channels. Reactant gases split their flow between the gas-diffusion electrodes and the channel exits, as determined by the current and the respective stoichiometry. Binary diffusion of hydrogen and water vapor occurs through the anode, and ternary diffusion of oxygen, nitrogen, and water vapor occurs through the cathode.

The flow of gas streams through the gas diffusion electrode is modeled in a manner similar to that described by Bernardi (7). Interdiffusion of gases through the porous electrode is calculated from tabulated data using the Stefan Maxwell equations with a Bruggemann correction

\* Electrochemical Society Active Member.

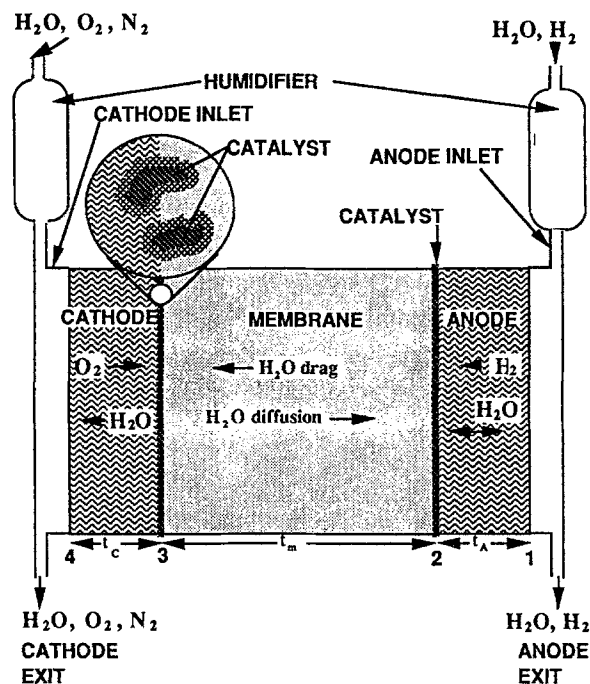


Fig. 1. Schematic diagram of fuel cell model.

applied to take account of the electrode porosity. The effect of the presence of water droplets is more difficult to treat rigorously. In this initial attempt at modeling water transport in the fuel cell, we deal with the droplet problem only qualitatively (see below).

Equilibrium of water activity is assumed at the electrode/membrane interface and determines the local amount of water at the membrane surface. An experimentally determined isotherm for water sorption into the membrane is used to convert from water vapor activity to water content in the membrane at the interface. The next flux of water across the membrane is calculated using the electro-osmotic drag and diffusion coefficients of water as functions of membrane water content.

When the equations that determine the water balance are solved, the membrane resistance and the  $O_2$  concentration at the catalyst interface are known. The cathode overpotential and a V-I curve for the fuel cell can then be determined. Anode catalytic activity is considered so high that anode overpotential is neglected. The onset of cathode flooding will precede any anode flooding. On the other hand, membrane drying near the anode could cause an extreme increase in the overall resistance. The active catalyst layer in the cathode is assumed to exist only as a thin plane at the cathode/membrane interface. The rest of the cathode serves only as a gas diffusion region.

### Mathematical Model

**Continuity equations in inlet flow channel.**—Figure 1 shows the five regions and the four interfaces of the model. When the constant cell current is  $J$  ( $A/cm^2$ ), the molar flux of  $H_2$  through the anode is  $I = J/2F$  mol/ $cm^2$ -s. Flows of  $H_2$  and water are considered to be positive when moving to the left toward increasing interface numbers. The  $O_2$  flow is positive in the opposite direction. Under steady-state conditions the  $N_2$  flow will always be zero. Fluxes and flow rates, designated  $N$ , are numerically identical between interfaces 1 and 4, because the cross-sectional area is unity. If  $\alpha$  is the ratio of the water flux crossing interface 1 (or 2) to the molar flux  $I$ , and  $N_{wA}$  and  $N_{wC}$  are the anode and cathode water flow rates (or fluxes) through interfaces 1 and 4, respectively, then the fluxes are all related by

$$I = J/2F = N_{H_2,1} = 2N_{O_2,4} = N_{wA}/\alpha = N_{wC}/(1 + \alpha) \quad [1]$$

The fluid composition in the anode and cathode flow channels is assumed to be uniform. The anode and cathode feed streams are each assumed to be saturated with water vapor at the humidifier temperatures, as

$$x_{wA}^1 = P_A^{\text{sat}}/P_A; x_{wC}^1 = P_C^{\text{sat}}/P_C \quad [2]$$

From flow balance, the anode inlet water flow less the exit water flow is the flow crossing interface 1

$$N_{wA}^1 - N_{wA}^L = N_{wA}; \frac{\nu_H x_{wA}^1 I}{1 - x_{wA}^1} - \frac{(\nu_H - 1)x_{w1} I}{1 - x_{w1}} = \alpha I \quad [3]$$

where  $\nu_H$ , the stoichiometric coefficient, is the ratio:  $N_{H_2}^1/N_{H_2,1}$ . On the cathode side there are three species. The inlet dry gas mole fraction of oxygen,  $x_{ON}$ , is known. The inlet  $O_2$  mole fraction of the saturated gas is  $x_O^1 = (1 - x_{wC}^1)x_{ON}$ . The three species inlet flow rates and exit flow rates expressed proportional to  $I$  are

$$N_{wC}^1 = \frac{x_{wC}^1 \nu_O I}{2(1 - x_{wC}^1)x_{ON}}; N_O^1 = \frac{\nu_O I}{2}; N_N^1 = \frac{\nu_O I(1 - x_{ON})}{2x_{ON}} \quad [4]$$

$$N_{wC}^L = N_{wC}^1 + (1 + \alpha)I; N_O^L = \frac{(\nu_O - 1)I}{2}; N_N^L = \frac{\nu_O I(1 - x_{ON})}{2x_{ON}} \quad [5]$$

The total cathode exhaust flow, obtained by summing the three exit flows in Eq. [5], are

$$N_{\text{total,C}}^L = \left[ \frac{\nu_O}{2(1 - x_{wC}^1)x_{ON}} + \alpha + \frac{1}{2} \right] I \quad [6]$$

The mole fraction of water and oxygen at interface 4 and throughout the cathode flow channel is the ratio of the water or oxygen flow to the total flow through interface 4. Thus

$$x_{w4} = \frac{x_{wC}^1 \nu_O + 2(1 + \alpha)(1 - x_{wC}^1)x_{ON}}{\nu_O + (2\alpha + 1)(1 - x_{wC}^1)x_{ON}}; \quad x_{O4} = \frac{(\nu_O - 1)(1 - x_{wC}^1)x_{ON}}{\nu_O + (2\alpha + 1)(1 - x_{wC}^1)x_{ON}} \quad [7]$$

Similarly, throughout the anode flow channel from Eq. [3] we get, for the mole fraction of water at interface 1

$$x_{w1} = \frac{\nu_H x_{wA}^1 - \alpha(1 - x_{wA}^1)}{x_{wA}^1 - \alpha(1 - x_{wA}^1) + \nu_H - 1} \quad [8]$$

The continuity conditions have given us  $x_{w1}$ ,  $x_{w4}$ , and  $x_{O4}$  as the input parameters and the (as yet unknown) ratio  $\alpha$  of water flux passing through interface 1 to flux  $I$ . Next we develop the equations for water transport through the two electrodes and the membrane. The region between interfaces 1 and 2 has binary diffusion of  $H_2$  and water vapor; the region between interfaces 2 and 3 has water drag of protonic current and water diffusion; and the region between interfaces 3 and 4 has ternary gas-phase diffusion.

**Gas diffusion in the electrodes.**—We assume that the anode and cathode gas mixtures with water vapor act as ideal gases. Let  $z$  increase in the direction of reactant flow, that is, from interface 1 to 2 and from interface 4 to 3. The Stefan-Maxwell equation for multicomponent diffusion defines the gradient in mole fraction of the components

$$\frac{dx_i}{dz} = RT \sum_j \frac{x_i N_j - x_j N_i}{PD_{ij}} \quad [9]$$

The binary diffusion coefficients were calculated for mass diffusivity from the Slattery and Bird (8) estimation at low pressures. The pressure-diffusivity product (atm-cm<sup>2</sup>/s) is estimated from critical temperature, critical pressure, and mass of the respective components A and B

$$P \cdot D_{AB} = a \left( \frac{T}{\sqrt{T_{cA} T_{cB}}} \right)^b (p_{cA} p_{cB})^{1/3} \quad (T_{cA} T_{cB})^{5/12} \left( \frac{1}{M_A} + \frac{1}{M_B} \right)^{1/2} \epsilon^{3/2} \quad [10]$$

where  $a = 0.0002745$ ,  $b = 1.832$  for  $H_2$ ,  $O_2$ , and  $N_2$ , and  $a = 0.000364$  and  $b = 2.334$  for water vapor. The  $\epsilon^{3/2}$  term is a Bruggemann correction of the diffusion coefficients to account for the porosity of the electrode (9).

This model assumes only concentration gradients, not total pressure gradients, across the electrodes. (A pressure drop can occur across the membrane if the anode and cathode pressures are different). From Eq. [9] we obtain the following differential equations for  $x_{wA}$  across the anode and for  $x_{wC}$  and  $x_{OC}$  across the cathode

$$\frac{dx_{wA}}{dz} = \frac{RTI}{P_A D_{wH}} [x_{wA}(1 + \alpha) - \alpha] \quad [11]$$

$$\frac{dx_O}{dz'} = \frac{RTI}{P_C} \left[ \frac{x_O(1 + \alpha) + 0.5x_{wC}}{D_{wO}} + \frac{1 - x_{wC} - x_O}{D_{ON}} \right] \quad [12]$$

$$\frac{dx_{wC}}{dz'} = -\frac{RTI}{P_C} \left[ \frac{(1 - x_{wC} - x_O)(1 + \alpha)}{D_{wN}} + \frac{0.5x_{wC} + x_O(1 + \alpha)}{D_{ON}} \right] \quad [13]$$

Equation [11] can be integrated across the anode thickness,  $t_A$ , from the initial condition of  $x_{wA} = x_{w1}$  at  $z = 0$  at interface 1, which we know from Eq. [8], to obtain  $x_{w2}$  at  $z = t_A$  at interface 2

$$x_{w2} = \left( x_{w1} - \frac{\alpha}{1 + \alpha} \right) \exp \left( \frac{RTI t_A}{P_A D_{wH}} \right) + \frac{\alpha}{1 + \alpha} \quad [14]$$

Similarly, Eq. [12] and [13] can be simultaneously integrated from the known initial conditions of Eq. [7] at interface 4 to obtain  $x_{O3}$  and  $x_{w3}$  at interface 3. Although these equations can be integrated analytically, we chose to integrate them numerically. We now have the water mole fraction in the gas mixture in contact with each side of the membrane in terms of  $\alpha$  and the input parameters and gas phase (electrode) transport parameters.

In this model we have not considered the possibility of large excesses of liquid water in the flow channels or within the electrode. In solving the continuity equations we did include, however, marginal situations in which a slight volume of liquid water forms within the channels of the electrodes. For the continuity equations, no distinction was made between water gas and water liquid molecules. If  $P_w$  exceeded  $P_{sat}$ , then the excess water was considered in the continuity equations as if it were finely dispersed droplets (with zero volume), having transport properties identical to those of water vapor. Only where the pressure of the reacting gas (oxygen) had to be considered for the cathode kinetics was the fraction of liquid water,  $x_{liq}$ , subtracted and the real mole fraction for gas phase alone was employed. Thus, the partial pressure of oxygen at the cathode is  $P_C x_{O3}/(1 - x_{liq})$ .

**Water transport in membrane.**—Membrane water content at the interface is determined by the activity of water vapor at the electrode/membrane interface, assuming equilibrium. The activity in the vapor phase is  $x_w P/P_{sat}$ . The saturation pressure of water,  $P_{sat}$ , used here and previously in Eq. [2] was fitted to the following empirical expression according to tabulated values (10)

$$\log_{10} P_{sat} = -2.1794 + 0.02953T - 9.1837 \cdot 10^{-5} T^2 + 1.4454 \cdot 10^{-7} T^3 \quad [15]$$

Membrane water content was measured by Zawodzinski *et al.*, (11) as a function of water activity for the Nafion 117 membrane by weighing membranes equilibrated above aqueous solutions of various lithium chloride concentrations. Figure 2 shows the resulting "isopiestic curve" measured at 30°C. Water content,  $\lambda$ , is given as the ratio of the number of water molecules to the number of charge

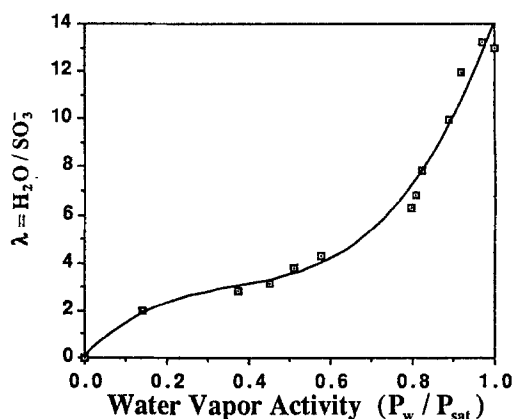


Fig. 2. Measured membrane water content vs. water activity for Nafion 117 at 30°C and according to Eq. [16].

( $SO_3H^+$ ) sites. A fit of the experimental relationship of  $\lambda$  vs. water vapor activity,  $a$ , used in the model is

$$\lambda_{(30C)} = 0.043 + 17.81a - 39.85a^2 + 36.0a^3 \text{ for } 0 < a \leq 1 \quad [16]$$

The measured value of  $\lambda$  in equilibrium with saturated water vapor at 30°C is 14  $H_2O$  per charged site (see Fig. 2). In the absence, at the moment, of isopiestic data at 80°C, we are assuming that the 30°C data applies to membrane equilibrium with water vapor at 80°C. Our measurements also show that when the membrane, following partial drying, is immersed in liquid water,  $\lambda$  can go as high as 22 when at water boiling temperature and to 16.8 when at 80°C. This apparent anomaly, in which water vapor and liquid water (in equilibrium with each other) equilibrate separately to different membrane water contents, is of theoretical and practical interest but will not be further discussed here. For modeling purposes, we allowed  $\lambda$  to increase linearly from 14 to 16.8 as the mole fraction of water exceeded saturation and increased from  $x_{w,sat}$  to  $3x_{w,sat}$ , that is, for

$$1 \leq \frac{x_w P}{P_{sat}} \leq 3, \lambda = 14 + 1.4 \left( \frac{x_w P}{P_{sat}} - 1 \right) \quad [17]$$

We measured, in Nafion 117, the number of water molecules dragged per  $H^+$  ion moved by electric field through the membrane and found it to be  $2.5 \pm 0.2$  for a fully hydrated membrane in equilibrium with liquid water at 30 or 50°C (12) (the membrane in these last experiments had been pretreated in boiling water). Based on work of LaConti *et al.* (13), we assume that the water drag coefficient is linearly proportional to water content. We have recently measured a value of only  $\sim 0.9$  water molecules dragged per  $H^+$  in partially hydrated Nafion with a water content  $\lambda$  of 11, which would indicate that this proportionality assumption will not underestimate water drag at low membrane water content. Thus, for the "complex"  $H^+(H_2O)_n$  migrating through the membrane at 80°C, we will designate the number of water molecules per proton as  $n_{drag}$ , and then

$$n_{drag} = 2.5\lambda/22 \text{ and } N_{w,drag} = n_{drag} \cdot (2I) \quad [18]$$

(The  $H^+$  flux ( $2I$ ) is twice the  $H_2$  flux,  $I$ .)

Using the pulsed-field gradient spin-echo nuclear magnetic resonance (NMR) technique, Zawodzinski *et al.* (11) also measured the intradiffusion coefficient of water in Nafion 117 membranes equilibrated over aqueous solutions of LiCl to set the water activity in contact with the membrane. We assume here that this intradiffusion coefficient,  $D'$ , relates a water diffusion flux to the gradient in chemical potential or the gradient in the logarithm of activity. In turn, the gradient, with respect to the laboratory coordinate  $z'$  of water content  $\lambda$  may be used

$$N_{w,dif} = -\frac{D'c_w}{RT} \nabla \mu = -\frac{D'c_w}{RT} \nabla (RT \ln a) = -D'c_w \frac{d(\ln a)}{d\lambda} \frac{d\lambda}{dz'} \quad [19]$$

In order to eliminate tracking the membrane swelling in the model, we convert to the equivalent water concentration in a dry membrane,  $\lambda_{\text{dry}}/M_m$ , and to a new coordinate,  $z$ , fixed to the dry membrane. To account for membrane swelling, dry membrane thickness dimensions are expanded by the factor  $(1 + s\lambda)$ . We define the corrected diffusion coefficient  $D_\lambda$ , which relates flux to gradient with respect to the dry membrane coordinates in water content  $\lambda$  and which is a function of  $\lambda$

$$N_{w,\text{dif}} = -D'c_w \frac{d(\ln a)}{d\lambda} \frac{d\lambda}{dz'} \\ = -D' \left( \frac{\lambda \rho_{\text{dry}}/M_m}{(1 + s\lambda)^2} \frac{da}{d\lambda} \right) \frac{d\lambda}{dz} = -\frac{\rho_{\text{dry}}}{M_m} D_\lambda \frac{d\lambda}{dz} \quad [20]$$

By differentiating the fit (at 30°C) of  $\lambda$  vs.  $a$ , from Eq. [16], to substitute for  $da/d\lambda$  in Eq. [20], the transformed diffusion coefficient for a coordinate fixed to the dry membrane is

$$D_{\lambda,30^\circ\text{C}} = \left( \frac{1}{(1 + s\lambda)^2} \frac{\lambda}{a(17.81 - 79.70\lambda + 108\lambda^2)} \right) D' \quad [21]$$

From the measured thickness of dry and fully hydrated Nafion 117 membranes, we determined  $s$  to have a value of 0.0126. Given  $\lambda$ , Eq. [16] is solved implicitly to determine  $a$  and is differentiated to get  $da/d\lambda$  for use in Eq. [21]. Figure 3 is a plot of  $D'$ ,  $D_\lambda$ , and their ratio as a function of Nafion 117 water content  $\lambda$ . The peak in the correction factor and in  $D_\lambda$  around  $\lambda = 3$  (Fig. 3) is very sensitive to the exact form of the strong variation in water activity in this region (see Fig. 2). In the model,  $D_\lambda$  was represented by a cubic polynomial for  $\lambda > 4$  and by tabular interpolation for  $\lambda \leq 4$ . Equation [22] is the fit for  $\lambda > 4$  of  $D_\lambda$  vs.  $\lambda$  at 30°C corrected, by an activation energy term, to the other temperatures we used

$$D_{\lambda>4} = 10^{-6} \exp \left[ 2416 \left( \frac{1}{303} - \frac{1}{273 + T_{\text{cell}}} \right) \right] \\ (2.563 - 0.33\lambda + 0.0264\lambda^2 - 0.000671\lambda^3) \quad [22]$$

The activation energy of Eq. [22] was based on measurements of Yeo and Eisenberg (14) on water diffusion in acid from Nafion of 1155 equivalent weight.

The net water flux through the membrane is

$$N_w = \alpha I = n_{\text{drag}} \cdot (2I) \cdot \frac{\lambda}{22} - \frac{\rho_{\text{dry}}}{M_m} D_\lambda \frac{d\lambda}{dz} \quad [23]$$

and hence

$$\frac{d\lambda}{dz} = \left[ 2n_{\text{drag}} \cdot \frac{\lambda}{22} - \alpha \right] \frac{IM_m}{\rho_{\text{dry}} D_\lambda(\lambda)} \quad [24]$$

Equation [24] can be integrated numerically from interface 2, where  $\lambda_2$  is determined by  $x_{w2}$  and Eq. [14]. This allows us to calculate  $\lambda_3$  and  $x_{w3}$ .

**Iterative solution.**—The key to solving the water transport through the PEFC occurs at this point, where we must apply in iteration to determine the proper value of  $\alpha$ . We distinguish  $x'_{w3}$ , which is obtained following the integration of Eq. [24], from  $x_{w3}$ , which is obtained following integration from the cathode end using Eq. [7] and [13]. These two values will be equal when the proper value of  $\alpha$  is used. This iteration includes Eq. [1]–[24], which were discussed in the three previous sections and which are all functions of  $\alpha$ .

**Membrane resistance and voltage drop.**—When the water profile in the membrane has been determined, we can determine the membrane resistance and the potential drop across it. The conductivity of Nafion 117 was measured above water for a range of water activities at 30°C. The conductivity was also measured at 30 and 80°C for a fully hydrated membrane from which an activation energy was

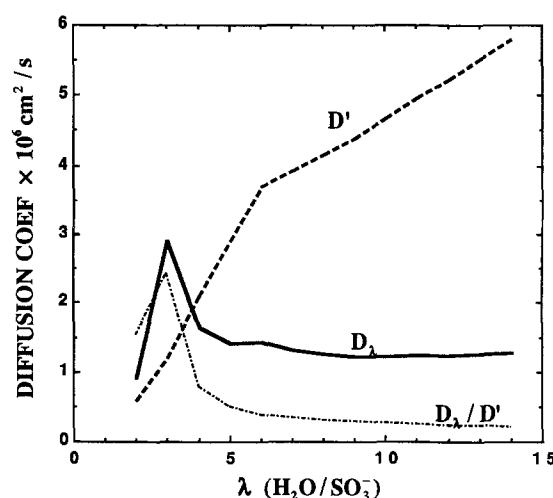


Fig. 3. Measured intradiffusion coefficient,  $D'$ , at 30°C, the corrected diffusion coefficient,  $D_\lambda$ , and the correction factor,  $D_\lambda/D'$ , calculated from measured activity and swelling, plotted against water content per charge site for Nafion 117.

found and assumed to apply at all values of  $\lambda$ . The following fit of conductivity in  $(\Omega\text{-cm})^{-1}$  as a function of  $\lambda$  was obtained

$$\sigma_{30} = 0.005139\lambda - 0.00326 \text{ for } \lambda > 1$$

$$\sigma(T_{\text{cell}}) = \exp \left[ 1268 \left( \frac{1}{303} - \frac{1}{273 + T_{\text{cell}}} \right) \right] \sigma_{30} \quad [25]$$

Below one water per charge site, the membrane conductivity was assumed constant. The membrane resistance in  $\Omega\text{-cm}^2$  is obtained using Eq. [24] and [25] by integration over the membrane thickness,  $t_m$ , as

$$R_m = \int_0^{t_m} \frac{dz}{\sigma(\lambda)} \quad [26]$$

**Cathode overpotential.**—To generate the complete cell polarization curve, we assume a cathodic overpotential loss in addition to the ohmic loss in the membrane. To calculate this cathode loss we used the simple Tafel expression for  $J$  vs.  $\eta$  given in Eq. [27]. Thus

$$J = j_o P_c \frac{x_{\text{O}_2}}{1 - x_{\text{liq}}} \exp \left[ \frac{0.5F}{RT} \eta \right] \quad [27]$$

where  $\eta = V_{\text{oc}} - V_{\text{cell}} - J \cdot R_{\text{mem}}$ . The exchange current density  $j_o$  is referenced to pure oxygen at 1 atm at the open cell potential  $V_{\text{oc}}$ . As mentioned earlier, the mole fraction of  $\text{O}_2$  is corrected to a gas-phase fraction. For the sake of simplicity, we do not consider in Eq. [27] the rather important effects of excess liquid water on oxygen mass transport rates within the cathode.

Because we initially specify the current density to get the water and oxygen concentrations and membrane resistance  $R_{\text{mem}}$ , Eq. [27] is solved implicitly to determine the value of  $V_{\text{cell}}$  (only positive voltage allowed) corresponding to the specified current density.

## Results and Discussion

The model has 16 input parameters plus specific isopiestic, diffusion, and electro-osmotic drag data that can vary for different membrane materials and many output variables that could be examined. We only focused on a few of these parameters and variables to illustrate the effects of water transport on the fuel cell system, as predicted by the assumptions of the model, and to observe which aspects of the model support and which fail to support certain experimental results. While developing the equations for the model, it was convenient to introduce  $\alpha$ , the ratio of net water flux to water flux produced at the cathode. To evaluate the model results, we will now use  $\beta$ , the net water flux

**Table I. The base-case input parameters and some computed variables for a cell with Nafion 117 membrane.**

Input parameters	Computed variables
$J = 0.5 \text{ A/cm}^2$	$V_{\text{cell}} = 0.668 \text{ V}$
$j = 0.01 \text{ A/cm}^2$	$R_{\text{mem}} = 0.285 \Omega\text{-cm}^2$
$v_{\text{H}} = 4$	$\alpha = 0.4$
$v_{\text{O}} = 6$	$\beta = 0.2 \text{ H}_2\text{O flux/H}^+ \text{ flux}$
$P_{\text{A}} = 3 \text{ atm}$	$x_{\text{w}1} = 0.1015$
$P_{\text{C}} = 3 \text{ atm}$	$x_{\text{w}2} = 0.1013$
$t_{\text{A}} = 0.0365 \text{ cm}$	$x_{\text{w}3} = 0.2327$
$t_{\text{C}} = 0.0365 \text{ cm}$	$x_{\text{w}4} = 0.2264$
$t_{\text{mem}} = 0.0175 \text{ cm}$	$x_{\text{O}3} = 0.1329$
$T_{\text{cell}} = 80^\circ\text{C}$	$x_{\text{O}4} = 0.1403$
$T_{\text{satA}} = T_{\text{satC}} = 80^\circ\text{C}$	$\text{Rel Hum}_1 = 0.6515$
$V_{\text{oc}} = 1.1 \text{ V}$	$\text{Rel Hum}_4 = 1.4535$
$x_{\text{O}N} = 0.21 \text{ (air)}$	$x_{\text{liq},4} = 0.077$
$x_{\text{wA}} = x_{\text{wC}} = 0.1558$	

per proton, which is simply  $0.5\alpha$ . The set of model parameters used for our base case is listed in Table I along with some of the computed variables for this case. When current density is varied,  $v_{\text{H}}$  and  $v_{\text{O}}$  are specified here for the maximum current density of  $2 \text{ A/cm}^2$  and inlet flow rates are held constant at this value (i.e.,  $v = v_{\text{max}} \cdot J_{\text{max}}/J$ ). Thus, in Table I, although  $v_{\text{H}}$  is 4 for a current density of  $0.5 \text{ A/cm}^2$ ,  $v_{\text{H}}$  will be 1 when the current density is increased to  $2 \text{ A/cm}^2$  at the same hydrogen flow rate.

For the base case, the anode and cathode gas streams both enter at saturated conditions. The relative humidity drops in the anode flow channel ( $x_{\text{w}1} < x_{\text{wA}}^1$ ) but forms additional liquid water in the cathode channel ( $x_{\text{w}4} > x_{\text{wC}}^1$ ). Figure 4 shows the computed water profile as a function of thickness fraction measured from the cathode on the left across the Nafion 117 membrane for four current densities. The  $J = 0.5 \text{ A/cm}^2$  curve, corresponding to the values of Table I, has a net water flux ratio  $\beta$  of 0.2 water molecules per  $\text{H}^+$  ion transported through the membrane. The net water flux moves from right to left or in the direction of increasing water content. At the higher current density there is more net water flux even though the ratio of net water flux per proton is less; thus, at the cathode, the values of  $\lambda$  vary from 14.1 to 15 as the current density increases from 0.1 to  $0.8 \text{ A/cm}^2$ . Some excess liquid is present at the cathode, so Eq. [17] describes the determination of  $\lambda$  at the membrane surface in the presence of excess liquid water at interface 3. The magnitude of the slope of the water profiles drops from cathode to anode, chiefly because the water drag flux is proportional to water content and, thus, less diffusion flux is required to offset it at steady state nearer the anode.

An examination of the water and oxygen mole fractions in Table I gives some insight into gas diffusion and the

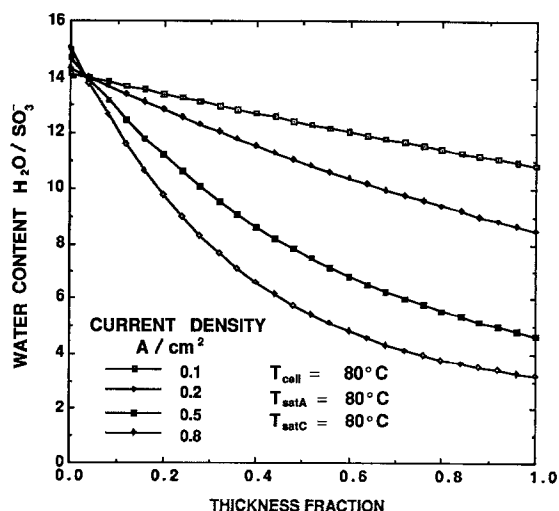


Fig. 4. Computed water profiles in Nafion 117 for the base case for four current densities holding gas flow rates constant,  $v_{\text{H}} = 1$  at  $1 \text{ A/cm}^2$ . The cathode is on the left, and the net water flux moves from right to left.

transport of water in the electrodes. Fully saturated water vapor enters both anode and cathode flow channels at 3 atm pressure,  $80^\circ\text{C}$ , corresponding to a water mole fraction of 0.1558. The membrane water flux leaving the anode flow channel and entering the membrane drops the remaining water vapor to a mole fraction,  $x_{\text{w}1}$  of 0.1015. This same membrane water flux, plus the water produced at the cathode, add to the mole fraction of water in the cathode and the cathode flow channel. Through the gas-diffusing anode, the mole fraction of water vapor drops very slightly to  $x_{\text{w}2}$  of 0.1013. These slight variations in anode gas composition between interfaces 1 and 2 (across the anode) mean that interplay between water and hydrogen gas transport across the anode are not significant for overall cell performance. In fact, considering interface 2 equivalent to interface 1 would be of little consequence. Unlike the case of the anode, across the cathode the water vapor flux diffuses counter to the oxygen flux, and the change in mole fraction across the cathode is not so slight. Because the initial cathode inlet stream was already saturated with water, excess liquid is present and is assumed to be thoroughly dispersed in the cathode and the cathode flow channel where the mole fraction of liquid water,  $x_{\text{liq},4}$ , is 0.077. Comparison of  $x_{\text{O}3}$  to  $x_{\text{O}4}$  (Table I) shows that the  $\text{O}_2$  pressure has dropped (at  $0.5 \text{ A/cm}^2$ ) only by about 5% across the cathode. This means that the limiting current set by oxygen diffusion through the cathode is about  $10 \text{ A/cm}^2$ .

Under different operating conditions, the model predicts good performance with no significant liquid water present. For example, referring to the previous base case, if the anode humidifier temperature is raised to  $105^\circ\text{C}$  while the cathode's is lowered to  $20^\circ\text{C}$  (cell temperature  $80^\circ\text{C}$ ) and the cathode stoichiometry is raised from 6 to 8.4, then the relative humidity is 0.914 in the anode flow channel and is 0.930 in the cathode flow channel. A very small amount of liquid is present at interface 3 ( $x_{\text{liq},3} = 0.0035$ ), but this evaporates during the diffusion path to interface 4. Examples are cited in which the cathode humidifier is at  $80^\circ\text{C}$  because, in the laboratory, less humidification to the cathode gave poor cell performance, contrary to such model predictions. We believe this is because of the partial drying of the membrane that apparently takes place because of the excessive evaporative loss through the graphite collector plates held at  $80^\circ\text{C}$ . When this "additional" cathode water removal path becomes understood, it will be included in future models.

Figures 5-9 display three variables (cell voltage,  $V_{\text{cell}}$ , membrane resistance,  $R_{\text{mem}}$ , and steady-state water-per-

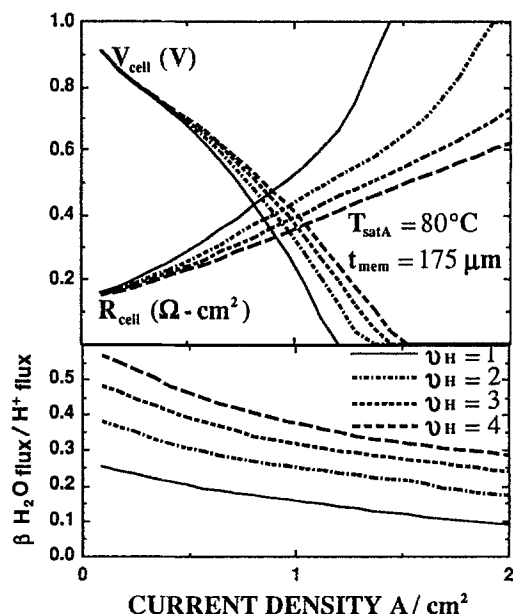


Fig. 5. Cell voltage, membrane resistance, and  $\text{H}_2\text{O}/\text{H}^+$  flux ratio vs. current density for different anode stoichiometry with anode humidifier at  $80^\circ\text{C}$ .

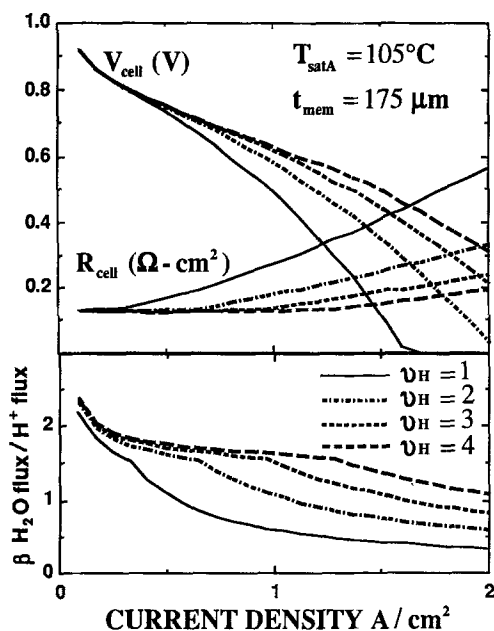


Fig. 6. Cell voltage, membrane resistance, and H<sub>2</sub>O/H<sup>+</sup> flux ratio vs. current density for different anode stoichiometry with anode humidifier at 105°C.

proton flux ratio, β) as a function of current density from 0 to 2 A/cm<sup>2</sup>. Except where indicated, all parameters correspond to the base case of Table I.

Figure 5 shows the effect on the base case of varying the anode stoichiometry. The only effect of variations in v<sub>H</sub> is through the role of H<sub>2</sub> as a carrier for water vapor in the inlet gas stream because the model assumes that overpotential occurs only at the cathode/membrane interface. Note that the steady-state water flux per H<sup>+</sup> ratio decreases with increasing current density for a fixed H<sub>2</sub> flow, and it increases with increased H<sub>2</sub> stoichiometry when more water vapor is supplied at the anode. A higher water flux results in lower membrane resistance and higher cell voltage at a given current density.

Figure 6 shows the effect of raising the anode humidifier temperature above the cell temperature. The membrane at low currents maintains a water content near 14 water molecules per membrane charge site throughout its thickness,

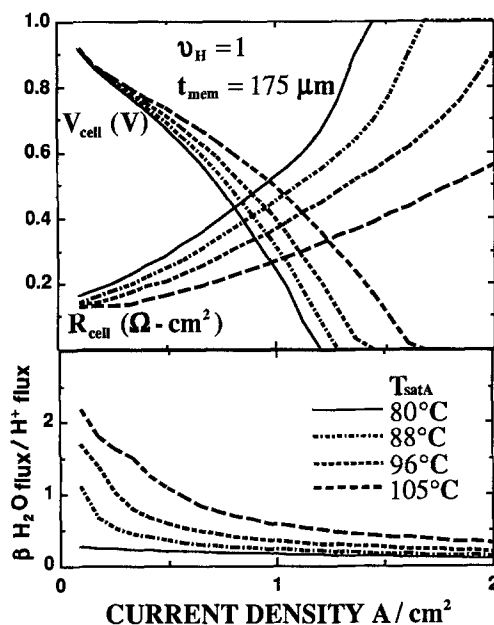


Fig. 7. Cell voltage, membrane resistance, and H<sub>2</sub>O/H<sup>+</sup> flux ratio vs. current density for different anode humidifier temperatures with anode stoichiometry of 1 at full current density.

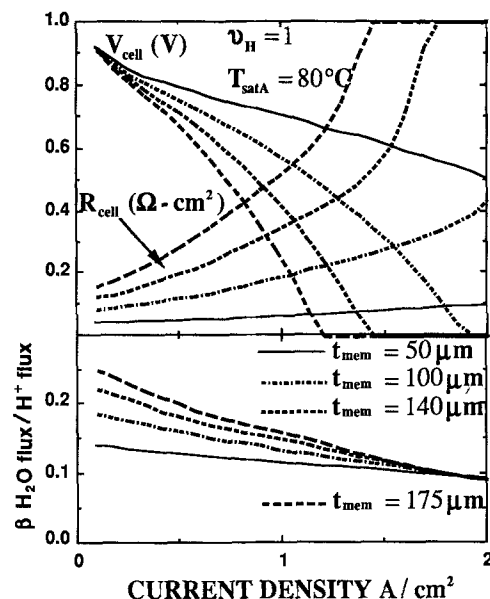


Fig. 8. V<sub>cell</sub>, R<sub>cell</sub>, and H<sub>2</sub>O/H<sup>+</sup> flux ratio β vs. J for four Nafion 117 membrane thicknesses at T<sub>satA</sub> = 80°C.

and the resistance approaches 0.13 Ω · cm<sup>2</sup>. The addition of more water vapor by raising the humidifier temperature has improved cell performance by lowering the membrane resistance considerably. This is clearly seen by comparing the cell resistance and cell polarization curves shown in Fig. 5 and 6. The initial high H<sub>2</sub>O/H<sup>+</sup> flux ratio β of about 2.3 at 0.1 A/cm<sup>2</sup> occurs because the 105-80°C difference in anode-to-cathode humidifier temperatures provides a gradient in membrane water content. (Remember that we allowed (in Eq. [17]) λ to increase with excess liquid water at the interface.) At higher current and lower v<sub>H</sub>, the flux ratio β drops. At v<sub>H</sub> = 1, we cannot transport much water vapor to the anode, which causes λ to drop in the membrane. This drops the electro-osmotic drag but also raises the resistance.

Figure 7 shows the effect of holding v<sub>H</sub> at 1 (defined for 2 A/cm<sup>2</sup>) and varying the temperature of the anode humidifier, T<sub>satA</sub>. Here the resistance increase with current is much higher than in Fig. 5, because less water is available from the anode feed stream for the membrane. The flux ratio β increases as T<sub>satA</sub> increases, principally because the

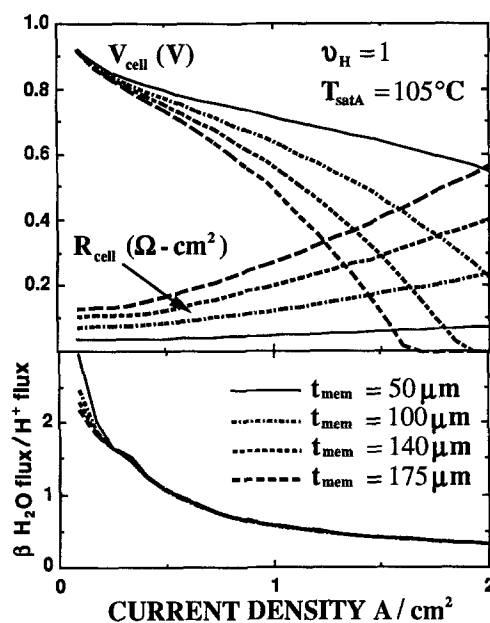


Fig. 9. V<sub>cell</sub>, R<sub>cell</sub>, and H<sub>2</sub>O/H<sup>+</sup> flux ratio β vs. J for four Nafion 117 membrane thicknesses at T<sub>satA</sub> = 105°C.

drag coefficient is proportional to  $\lambda$ . The inflections observed near  $\beta = 1.59$  occur because the slope of the  $\lambda$  vs. water activity curve changes when the water vapor at the interface reaches saturation. (The value of  $n_{\text{drag}}$  is 1.59 at  $\lambda = 14$ .) In general, the value of  $\beta$  is less than  $n_{\text{drag}}$  because backdiffusion ameliorates the effect of the electro-osmotic drag.

Figure 8 shows the significant advantage of thinner membranes. At  $T_{\text{satA}} = 80^\circ\text{C}$ , four membrane thicknesses are compared. With the thin  $50\text{ }\mu\text{m}$  membrane, not only is the resistance less than  $0.05\text{ }\Omega\text{-cm}^2$ , but the flux ratio  $\beta$  is very low compared with the drag coefficient. Thus, the need to continuously replenish the anode with water from the cathode in real stack operation becomes much smaller. The backdiffusion of water is now able to supply the anode need. Figure 9 shows the effect of the same membrane thickness variation but at an anode humidifier temperature of  $105^\circ\text{C}$ . Now the steady-state gradient of membrane water content keeps the resistance lower for the thicker membranes, but it also causes more water to move to the cathode.

We performed several measurements to verify the predictions of the water transport aspects of this model. In the first measurement we collected water from the outlet gas streams of a  $50\text{ cm}^2$  cell with a 117 Nafion membrane, using Prototech electrodes, and compared it with the inlet streams. We found at  $500\text{ mA/cm}^2$  that  $0.2\text{ H}_2\text{O}$  was transported per  $\text{H}^+$  at  $80^\circ\text{C}$ .

The second type of measurement was that of high-frequency resistance ("ohmic resistance") of a  $1\text{ cm}^2$  Nafion 117 cell operating on air and hydrogen at  $80^\circ\text{C}$  cell and humidifier temperatures, and at 3 atm anode pressure and 5 atm cathode pressure. The anode-cathode high-frequency resistance is measured at 5 kHz, where concentration polarization and faradaic effects are eliminated, leaving, presumably, only the membrane resistance and any contact resistance. Figure 10 shows that both the experiment and the model indicate an increase in high-frequency resistance ( $R_{\text{HF}}$ ) with cell current. When the anode and cathode humidifier temperatures were raised to  $105^\circ\text{C}$  the high-frequency resistance actually decreased slightly with current density. We do not yet understand the observed dependence of  $R_{\text{HF}}$  on cell current when the cell is well humidified ( $T_{\text{sat}} = 105^\circ\text{C}$ ).

Some general comments about the approach described in this manuscript are in order. We would like to stress again the strong reliance, in this modeling effort, on membrane parameters that have been measured in our laboratory. We believe that in the effort to model a complex system such as this, where the results depend on so many model parameters, the results of the code are of little value unless they rely to the maximum extent possible on experimentally derived parameters. In this context, let us briefly

review the experiments performed, to highlight several aspects. The isopiestic technique has been shown here and elsewhere (11) to provide a good basis for establishing a range of well-defined water contents in the ionomeric membrane, allowing us to derive the dependence of membrane protonic conductivity and water diffusion coefficient on water content. Water (intra)diffusion coefficients have been derived over a range of membrane water contents using the  $^1\text{H}$ -pulsed gradient spin-echo (PGSE) NMR technique (11). The  $^1\text{H}$  intradiffusion coefficient was found to vary across a full order of magnitude as the membrane water content varies between 2 and 14 water molecules per sulfonate group. From arguments of  $\text{H}_2\text{O}/\text{H}^+$  population ratio in the membrane at high water contents and from similar apparent values of  $D$  derived from NMR and from protonic conductivity at small membrane water contents, we conclude that the NMR measured  $D$  of  $^1\text{H}$  is very close to  $D_{\text{H}_2\text{O}}$  in the range of water contents probe (11). We do intend, however, to further test the full accuracy of this conclusion in some future  $^{17}\text{O}$  NMR experiments.

Another subtle aspect needs to be mentioned in the context of applying an intradiffusion coefficient, (as derived from NMR or from a radioisotope labeling experiment), as an interdiffusion coefficient, that is, using the intradiffusion coefficient in a Fick's first law formalism (see Eq. [19]). In a strict analysis the intradiffusion coefficient (NMR) and the interdiffusion coefficient (Eq. [19]) are not necessarily identical (15). However, to complete this stage of work on the PEFC model, we felt that the proton diffusion coefficient derived by NMR as a function of membrane water content can yield, upon correction for activity coefficient, a satisfactory approximation for the interdiffusion coefficient of water in the membrane. The values we obtained for the intradiffusion coefficient of water are reasonable; they fall between one order of magnitude smaller (for a fully hydrated membrane) and two orders of magnitude smaller (for a membrane with  $\lambda = 2$ ) than the intradiffusion coefficient of water in liquid water, and they are in general agreement with other reported values of  $D(\text{intra})$  at high (2-4) and very low (16) water contents. In fact, when the water activity gradient is used in a Fick's first law expression (Eq. [19]), the effect  $D$  becomes almost independent of water content (Fig. 3), at a level of  $1.2 \cdot 10^{-6}\text{ cm}^2/\text{s}$ . This, again, is a very reasonable result for the diffusion coefficient of water in a water-absorbing ionomeric membrane like Nafion. It is similar in magnitude to that reported by Yeo and Eisenberg (14) for measurements under interdiffusion conditions. The reasonable order of magnitude of  $D_{\text{water}}$  evaluated here is stressed because, in other previous contributions, much higher values of  $D_{\text{water}}$  were mentioned. In fact,  $D_{\text{water}}$  higher than the diffusion coefficient of water in liquids at the same temperature was invoked (6). Such large values of  $D_{\text{water}}$  were required to explain experimental observations, because it was assumed (4, 6) that the electro-osmotic drag is not lowered as the membrane water content becomes smaller. Our results show clearly that experimental observations can be fully accounted for with the apparently very conservative levels of  $D_{\text{water}}$  in the membrane. These observations are based on the NMR measurements and their interpretation. The capability to account for observed cell performance with such conservative water diffusion coefficients is, in turn, based on the lowering of the electro-osmotic water drag in the membrane with the lowering in membrane water content (Eq. [18]). It is the interplay between the diffusion coefficient of water and the degree of water drag, including the variations of these two parameters with membrane water content, which, together, determine the water profile in the membrane under given humidification conditions and cell current density.

In the context of the latter point, we would like to stress the difference between the electro-osmotic drag, designated by  $n_{\text{drag}}$  in this paper, and the steady-state flux ratio  $\text{H}_2\text{O}/\text{H}^+$  designated by  $\beta$  because these two parameters have sometimes been intermixed in previous discussions of this system. It should be clear that  $n_{\text{drag}}$  is what one measures for a membrane fully immersed in liquid water, when the electro-osmotic drag is recorded at unit activity

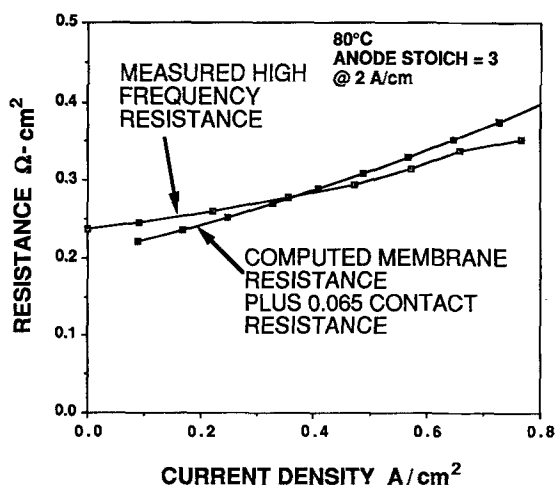


Fig. 10. Measured high-frequency resistance of a fuel cell with Nafion 117 compared with model membrane resistance plus  $0.065\text{ }\Omega\text{-cm}^2$  resistance. The cathode pressure was raised to 5 atm (3 atm on anode) to squeeze the membrane and electrodes.



of water throughout the system. On the other hand, in a fuel cell operating at steady state at a certain current density, there would be usually a significant gradient of water content (see Fig. 4), and, hence, the measured flux of water from anode compartment to cathode compartment per proton passed through the membrane  $\beta$  would be significantly smaller than  $n_{\text{drag}}$  (see Eq. [23]). This distinction between  $\beta$  and  $n_{\text{drag}}$  has significant practical implications in the context of the extent of "back-pumping" of water from cathode to anode, which would be required during steady-state cell operation. It should be clear that the level of water recirculation required is given by  $\beta$ , not by  $n_{\text{drag}}$ , and thus is significantly lower than would be suggested by naive inspection of only  $n_{\text{drag}}$ .

Finally, we should bring up two discrepancies between the real PEFC system with which we have experimented and the validity domain of this model. One noticeable discrepancy is that the model does not predict the need to humidify the cathode feed stream continuously at any appreciable current density. In practice, however, we found that in cells based on the Nafion 117 membrane, the highest performance is obtained only with well-humidified cathode feed streams. We believe that this is because evaporative water losses from the cell are substantial, in practice, at least in our test cell configurations. Unless supplied with an aerosol of water ( $T_{\text{sat}} = 105^\circ\text{C}$ ), the membrane loses water at an excessive rate, which cannot be compensated by water production at the cathode. This evaporative loss is not considered in our model at present, and, therefore, the model does not predict the need for extensive cathode humidification. On the other hand, as stressed before, the model does not consider the effect of substantial excess of liquid water in the cathode. One important effect expected is an additional thin film diffusion barrier for reactant gas transport (17). Such an excess of liquid water may be essential, however, to achieve the highest degree of membrane hydration, and, thus, the highest possible protonic conductivity. How to compromise between these two conflicting effects of excess liquid water at the cathode is a key to the successful operation of a PEFC.

### Conclusions

We developed a simple, one-dimensional, isothermal model of a complete polymer electrolyte fuel cell that has provided useful insight into the cell's water transport mechanisms and their effect on the cell's performance. We applied equilibrium conditions between membrane water and electrode water vapor at the membrane/electrode interfaces and considered the electro-osmotic and diffusion driving forces for water in the membrane and diffusion for water vapor and reactant gases in the electrodes to obtain material balances throughout the cell. The model used data that we measured for 117 Nafion membranes, including water content *vs.* water activity and water diffusion coefficient, protonic conductivity, and electro-osmotic water drag as a function of membrane water content.

The model was designed for water in the vapor state in the electrodes, but it could accommodate some excess liquid water assumed to be very finely dispersed. Experimental verification of some of the model predictions was successful when the measured cell was operated under conditions in which excess liquid was not present in the cathode. Measured net steady-state water flux per  $\text{H}^+$  in a  $50\text{ cm}^2$  cell of  $0.2\text{ H}_2\text{O}/\text{H}^+$  agrees with model predictions at  $80^\circ\text{C}$  cell and humidifier temperatures. Likewise, the measured high-frequency resistance of a  $1\text{ cm}^2$  cell at an  $80^\circ\text{C}$  humidifier temperature increased with current density, as the model predicted. This effect was not observed when a  $105^\circ\text{C}$  humidifier temperature was used.

An important conclusion is that the net water per  $\text{H}^+$  flux ratio in a PEFC can be as little as one-tenth of the electro-osmotic drag coefficient measured for a fully hydrated membrane, thus reducing the problem of water management for PEFC stacks.

### Acknowledgments

We wish to acknowledge our many fruitful discussions with Mr. Thomas Fuller, who contributed to the development of the work described herein. This work was sup-

ported by the U.S. Department of Energy, Office of Conservation and Renewable Energy.

Manuscript submitted Dec. 10, 1990; revised manuscript received Feb. 11, 1991.

Los Alamos National Laboratory assisted in meeting the publication costs of this article.

### LIST OF SYMBOLS

#### Subscripts

1	anode plenum to anode interface
2	anode electrode to membrane interface
3	membrane to cathode interface
4	cathode to cathode plenum interface
A	anode region, or component A
B	component B
C	cathode region
H	hydrogen, $\text{H}_2$
N	nitrogen, $\text{N}_2$
O	oxygen, $\text{O}_2$
mem	membrane
sat	saturation
w	water

#### Superscripts

I	initial value entering inlet flow channels
L	final value leaving inlet flow channels

#### Parameters and variables

$D$	diffusion coefficient, $\text{cm}^2/\text{s}$
$F$	Faraday constant, 96,484 C/mol
$I$	water molar flux produced at cathode $J/2F$ , mol/ $\text{cm}^2\text{ s}$
$J$	current density, $\text{A}/\text{cm}^2$
$M_m$	equivalent weight of membrane
$M_w$	molecular weight of water
$n_{\text{drag}}$	electro-osmotic drag coefficient
$N$	molar flux, $\text{mol}/\text{cm}^2\text{ s}$
$p_c$	critical pressure, atm
$P$	pressure, atm
$R$	molar gas constant
$R_{\text{cell}}$	membrane resistance, $\Omega\text{ cm}^2$
$t$	thickness, cm
$T$	temperature, $^\circ\text{C}$
$T_c$	critical temperature, K
$V$	cell potential, V
$x$	mole fraction
$z$	distance variable, cm
$\alpha$	ratio of net $\text{H}_2\text{O}$ flux in membrane to $\text{H}_2\text{O}$ flux product at cathode
$\beta$	ratio of net $\text{H}_2\text{O}$ flux in membrane to $\text{H}^+$ flux in membrane
$\lambda$	water content or local ratio $\text{H}_2\text{O}/\text{SO}_3^-$ in the membrane
$\rho$	density, $\text{g}/\text{cm}^3$
$\nu$	stoichiometric coefficient

### REFERENCES

1. R. A. Lemons, *J. Power Sources*, **29**, 251 (1990).
2. M. Verbrugge and R. Hill, *J. Phys. Chem.*, **92**, 6778 (1988).
3. M. Verbrugge, *This Journal*, **136**, 417 (1989).
4. R. Hill and M. Verbrugge, *ibid.*, **137**, 886 (1990).
5. J. L. Fales, N. E. Vanderborgh, and P. Stroeve, in "Diaphragms, Separators, and Ion-Exchange Membranes," J. W. van Zee, R. E. White, K. Kinoshita, and H. S. Burney, Editors, PV 86-13, p. 179, The Electrochemical Society Softbound Proceedings Series, Pennington, NJ (1986).
6. T. Fuller and J. Newman, in "Fuel Cells," R. E. White and A. J. Appleby, Editors, PV 89-14, p. 25, The Electrochemical Society Softbound Proceedings Series, Pennington, NJ (1984).
7. D. Bernardi, *ibid.*, p. 51.
8. J. C. Slattery and R. B. Bird, *AIChE J.*, **4**, 137 (1958).
9. R. E. De La Rue and C. W. Tobias, *This Journal*, **106**, 827 (1959).
10. "Handbook of Chemistry and Physics," 62nd ed., CRC Press, Boca Raton, FL (1981).
11. T. Zawodzinski, M. Neeman, L. Sillerud, and S. Gottesfeld, *J. Phys. Chem.*, Submitted.
12. C. Derouin, J. Pafford, S. Radzinski, T. Springer, and S. Gottesfeld, Abstract 627, p. 903, The Electrochemical Society Extended Abstracts, Vol. 89-1, Los Angeles, CA, May 7-12, 1989.



13. A. B. LaConti, A. R. Fragala, and J. R. Boyack, in "Electrode Materials and Processes for Energy Conversion and Storage," J. D. E. McIntyre, S. Srinivasan, and F. G. Will, Editors, PV 77-6, p. 354, The Electrochemical Society Softbound Proceedings Series, Pennington, NJ (1977).
14. S. C. Yeo and A. Eisenberg, *J. Appl. Polym. Sci.*, **21**, 875 (1977).
15. J. Crank, "The Mathematics of Diffusion," 2nd ed., Clarendon, Oxford (1975).
16. T. Nguyen, J. C. Hedstrom, and N. Vanderborgh, in "Fuel Cells," R. White and A. Appleby, Editors, PV 89-14, p. 39, The Electrochemical Society, Softbound Proceedings Series, Pennington, NJ (1989).
17. T. E. Springer and I. D. Raistrick, *This Journal*, **136**, 1594 (1989).

## Measurements of Double-Layer Capacitance at the Preoxidized Ni/Fused Na<sub>2</sub>SO<sub>4</sub> Interface

Yiing-Mei Wu\*,<sup>1</sup>

Department of Materials Science and Engineering, The Ohio State University, Columbus, Ohio 43210

### ABSTRACT

The double-layer capacitance in a fused Na<sub>2</sub>SO<sub>4</sub> film on a preoxidized Ni electrode at 1200 K was measured by electrochemical impedance spectroscopy. The capacitance-potential curve has a maximum at a potential of -0.6 V vs. Ag/Ag<sub>2</sub>SO<sub>4</sub>, silica reference electrode, resulting from the additional contribution of a faradaic reaction.

Most of the studies of double-layer properties have been conducted on metal electrodes in aqueous solutions (1-5). Only a few researchers investigated the capacitance (C)-potential (E) relation in molten salt electrolytes. Graves and Inman (6) have reviewed the case for a liquid lead electrode in KCl-LiCl melts. The capacitance is thought to comprise both the double layer and faradaic contributions. The shape of the C-E curve is parabolic with a minimum at the  $E_{pzc}$  (potential of zero charge). More recently, Painter *et al.* (7) used a model of charged hard sphere fluid in contact with a charged hard electrode wall to explain the features of the capacitance for the metal/molten salt (alkali halides) interface. Although the magnitude of the calculated capacitance is comparable with experimental values, the temperature dependence of capacitance at  $E_{pzc}$  cannot be reproduced by the hard sphere model. This probably arises from "relaxation" of the structure, especially near the metal/molten salt interface, where the interactions between metal-ion and ion-ion are strongest.

In the current study, the capacitance in a fused Na<sub>2</sub>SO<sub>4</sub> film on a preoxidized Ni electrode was measured by electrochemical impedance spectroscopy. With an appropriate equivalent circuit, obtaining capacitance values from impedance measurements is straightforward and accurate, as compared to other pulse methods (8). This system was chosen because of its relevance to the hot corrosion degradation of metals or alloys in gas turbines and other fuel combustion systems. Furthermore, as the development of the molten salt fuel cells and batteries advances, the need for information on the structure of the electrode/molten salt interface has become rather urgent. Double-layer capacitance, among other surface properties, is an important and experimentally accessible parameter in that respect.

### Experimental Procedure

Thin film impedance measurement at 1200 K were carried out using the apparatus and procedures reported earlier (9). The working electrode (WE) was a 99.9975% pure preoxidized Ni wire wound around the outer surface of an yttria-stabilized zirconia reference electrode (RE). A platinum foil counterelectrode (CE) encircled the zirconia RE without touching the preoxidized nickel WE. The space between the CE and WE was made small (about 2 mm) so that a thin layer of used salt could be held there during an experiment. A fused silica reference electrode also con-

tacted the nickel WE to act as the second RE. The combination of the zirconia and silica reference electrodes provided measures for both the basicity and oxygen pressure at the WE. The Ni WE was preoxidized in pure oxygen at 1200 K for 2 h, resulting in an oxide thickness of 4.3  $\mu$ m. After this preoxidation, Ni WE arrangement was immersed briefly into fused Na<sub>2</sub>SO<sub>4</sub> contained in a silica crucible, and the gas atmosphere was changed to a catalyzed 0.1% SO<sub>2</sub>-O<sub>2</sub> gas mixture. Upon withdrawal of the sample from the melt, a thin fused salt film covered the electrodes. The thickness of the fused salt film between the WE and CE was about 2 mm. The previous study (9) had shown that the WE was passive under these conditions, i.e., the salt film did not directly contact the Ni metal substrate.

Electrochemical impedance measurements were performed with a Princeton Applied Research (PAR) 5208 two-phase lock-in analyzer and a PAR 273 potentiostat interfaced through an IEEE 488 bus to an IBM PS-2 computer. This system generated a sinusoidal voltage which was applied to the WE with a maximum amplitude less than 10 mV for frequencies ranging from 10<sup>-3</sup> to 10<sup>5</sup> Hz. A fast Fourier transform (FFT) technique was employed for frequencies from 10<sup>-3</sup> to 10 Hz to increase measurement speed and lower the degree of perturbation to the cell. Through use of the potentiostat, polarization of the WE with respect to the silica RE was performed and impedance measurements were made after the polarization current was stabilized (change of less than 10% per 10 min). Impedance data were stored and plotted by the computer. Potentiodynamic polarization was conducted with the same potentiostat in a separate experiment. The scan rate was 1 mV/s.

### Results and Discussion

Figure 1 shows the typical impedance spectrum at the open-circuit potential and the corresponding equivalent circuit, which were reported earlier (9). In Fig. 1, the low-frequency Warburg impedance corresponds to the diffusion of oxidant, S<sub>2</sub>O<sub>7</sub><sup>2-</sup>, in the thin salt film

$$W_o = \sigma_o \omega^{-1/2} (1 - j), \quad j = \sqrt{-1} \quad [1]$$

where  $\sigma_o$  is the Warburg coefficient, as shown in the equivalent circuit in Fig. 1,  $\omega = 2\pi f$  and  $f$  is the frequency. The two semicircles at medium and high frequencies were attributed to the impedance for the charge transfer at the oxide-salt interface,  $R_{o/s}$ , and the resistance to the movement

\* Electrochemical Society Student Member.

<sup>1</sup> Present address: Mobil Research and Development Company, Paulsboro, New Jersey 08066-0486.